Atmos. Chem. Phys. Discuss., 8, 5813–5845, 2008
www.atmos-chem-phys-discuss.net/8/5813/2008/

Atmospheric Chemistry and Physics Discussions

Parameterization of sea-salt optical properties and physics of the associated radiative forcing

J. Li[1], **X. Ma**[1], **K. von Salzen**[1], **and S. Dobbie**[2]

[1]Canadian Centre For Climate Modelling and Analysis, Science and Technology Branch, Environment Canada, University of Victoria, Victoria, British Columbia, Canada
[2]Inst. for Atmospheric Science, School of Earth and Environment, Univ. of Leeds, Leeds, UK

Received: 20 December 2007 – Accepted: 16 February 2008 – Published: 19 March 2008

Correspondence to: J. Li (jiangnan.li@ec.gc.ca)

Published by Copernicus Publications on behalf of the European Geosciences Union.

Abstract

The optical properties of sea-salt aerosol have been parameterized at solar and longwave wavelengths. The optical properties were parameterized in a simple functional form in terms of the ambient relative humidity based on Mie optical property calculations. The proposed parameterization is tested relative to Mie calculations and is found to be accurate to within a few percent. In the parameterization, the effects of the size distribution on the optical properties are accounted for in terms of effective radius of the sea-salt size distribution. This parameterization differs from previous works by being formulated directly with the wet sea-salt size distribution (and compared to AERONET results) and, to our knowledge, this is the first published sea-salt parameterization to provide a parameterization for both solar and longwave wavelengths.

We have used this parameterization in a set of idealized 1-D radiative transfer calculations to investigate the sensitivity of various attributes of sea-salt forcing, such as dependence with sea-salt column loading, effective variance, solar angle, and surface albedo. From these sensitivity tests, it is found that sea-salt forcings for both solar and longwave spectra are linearly related to the sea-salt loading for realistic values of loadings. The radiative forcing results illustrate that the shortwave forcing is an order of magnitude greater than the longwave forcing results and opposite in sign, for various loadings. Studies of the sensitivity of forcing results to variations in effective variance show there to be minimal variation; therefore, only one value of effective variance is used in the parameterization. The dependence of sea-salt forcing with solar angle illustrates an interesting result that sea-salt can generate a positive top-of-the-atmosphere result (i.e. warming) when the solar zenith angle is relatively small 30°. Finally, it is found that the surface albedo significantly affects the solar radiative forcing, with the forcing diminishing to zero as the surface albedo tends to unity.

We anticipate this new sea-salt optical property parameterization will be useful for GCM models due to its simplicity, computational efficiency, and that its sensitivities have been explored and summarized in this work.

ACPD

8, 5813–5845, 2008

1 Introduction

In the last several decades, interest in sea-salt aerosol has increased, partly because it is essential for explaining a significant portion of the differences in clear-sky top-of-the-atmosphere irradiance between observations and modeling results over the oceans (Haywood et al., 1997; Li et al., 2006). Globally and annually averaged, sea-salt dominates the radiative transfer in the marine atmosphere compared to all other types of aerosol in terms of the outgoing solar irradiance at the top-of-the-atmosphere. Accurate sea-salt radiative properties are not only important for the energy budget of the present-day atmosphere, they are also important for understanding both past and future climate change as well. As examples, consider that during the Younger Dryas period, sea-salt concentrations were higher than at present by a factor of about three (Alley , 2000). By the end of this century, IPCC scenarios are predicting an increase in sea-salt burden based on future global wind patterns and strengths. This might entail an estimated additional $-0.8\,\mathrm{W/m^2}$ direct sea-salt forcing and $-1.16\,\mathrm{W/m^2}$ indirect forcing (Penner et al., 2001). However, considerable uncertainties exist with regard to the magnitude of the sea-salt radiative forcing, especially the indirect forcing. For example, an increase in sea-salt concentrations in the marine boundary layer may lead to either increased or reduced cloud droplet number concentrations, depending on the amount of sulphate aerosol and meteorological situation (e.g., O'Dowd et al., 1999).

The radiative forcing from sea-salt affects a variety of processes such as sensible and latent heat fluxes and consequently the static stability of the atmosphere and its general circulation. Although, solar parameterizations of sea-salt optical properties exist Dobbie et al. (2003) Winter and Chylek (1997), no parameterization of sea-salt optical properties appear in the literature for the longwave yet, as they do for example for sulphates (Li and Min, 2002) and black carbon and organic carbon (Bäumer et al., 2007). Dobbie et al.'s approach is based on a two-mode scheme which separates the sea-salt size distribution into separate particle size categories for accumulation mode and coarse mode sea-salt. Here, a new parameterization for sea-salt longwave and

ACPD
8, 5813–5845, 2008

shortwave optical properties is proposed. The approach is based on the assumption of variable sea-salt size distributions and an updated treatment of solar optical properties.

Sea-salt particles grow (shrink) in size as relative humidity increases (decreases) (Tang et al., 1997) changing not only size but also composition. A key aspect of the work has been to provide an accurate representation of the response of sea-salt optical properties and radiative forcings to changes in relative humidity. In many models, aerosol optical properties are either fixed or based on the dry aerosol size distribution for two specified particle size modes with a corresponding growth factor taken at a representative humidity. In contrast, it is proposed here to directly consider the size distribution of the wet sea-salt aerosol particles for optical properties. This method has the advantage over previous methods by being more precisely based on the underlying physics related to the sea-salt size distribution.

To understand the physics for the aerosol radiative forcing, we implemented the proposed parameterization scheme in a 1-D column radiative transfer model. We investigated the sensitivity of the simulated forcing to variations in effective radius, effective variance, surface albedo and solar angle. In contrast to other studies based on global climate models, this approach allows a more rigorous evaluation of fundamental aspects of sea-salt radiative forcing.

2 Sea-salt growth rate and size distribution

Sea-salt is generated at the ocean surface by various processes, including bubble bursting and the generation of spume droplets. The bursting of bubbles and subsequent ejection of jet droplets into the air represents a major source of sea-salt particles. The jet droplets are solutions of water and sodium chloride and other minor organic compounds. In this study, the sea-salt composition is the same as that assumed by (Tang et al., 1997). Further discussions of sea-salt production and properties can be found in Lewis and Schwartz (2004).

After injection, the solution droplets will either grow or evaporate until thermodynamic

equilibrium with the atmosphere is reached. As the particle size varies with respect to the environmental relative humidity, the concentrations of the solutes in the aerosol particles will vary accordingly, affecting the aerosol mass density, surface tension, refractive indexes, and optical properties.

The size distribution of sea-salt aerosol tends to closely resemble a log-normal distribution, i.e.,

$$n(r) = \frac{dN}{dr} = \frac{N_0}{\sqrt{2\pi} r \ln\sigma} \exp\left[-\frac{(\ln r - \ln r_0)^2}{2(\ln\sigma)^2}\right] . \quad (1)$$

In Eq. (1), r is the radius of the aerosol particle, N_0 is the total number density, r_0 is the geometric mean radius and σ is the geometric standard deviation. The effective radius and effective variance for the log-normal distribution are easily obtained as

$$r_e = \frac{\int_0^\infty n(r) r^3 dr}{\int_0^\infty n(r) r^2 dr} = r_0 \exp[2.5(\ln\sigma)^2] \quad (2)$$

and

$$v_e = \frac{\int_0^\infty (r - r_e)^2 r^2 n(r)\, dr}{r_e^2 \int_0^\infty r^2 n(r)\, dr} = \exp[(\ln\sigma)^2] - 1. \quad (3)$$

In the Canadian Centre for Climate Modelling and Analysis (CCCma) GCM, the sulphate aerosol size distribution has previously been simulated based on a bin method (Ma and von Salzen, 2006) and also based on the more efficient piecewise log-normal approximation (PLA) method (von Salzen, 2006). According to the PLA method, pieces of different log-normal distributions are used within separate sections of the particle size spectrum for a realistic and flexible representation of aerosol size distributions. A smaller number of size sections can be used in simulations with the PLA method compared to the bin method. This results in a numerically more efficient and accurate treatment of aerosol size distributions in atmospheric models.

ACPD
8, 5813–5845, 2008

In Fig. 1, the upper panel shows observed aerosol size distributions according to AERONET (Holben et al., 1998) for a large number of sites around the world. The lower panel only shows the results for ocean sites. An important feature for the observed size distribution in Fig. 1 is the bi-modal shape. The different modes are usually associated with different types of aerosol. The small mode typically corresponds to sulfate aerosol, and the large mode to sea-salt and mineral dust. However, from the available observations it is not straightforward to distinguish between different types of aerosol, including sea-salt. In addition, simulated sea-salt distributions from an experimental version of the CCCma AGCM (Ma et al., 2008) are shown for the same locations as the AERONET observations in Fig. 1. It is found that the simulated sea-salt distribution matches reasonably well with the large mode distributions from the AERONET observations, especially for the ocean sites.

Fig. 2 shows vertical profiles of the aerosol effective radius and effective variance for globally averaged values over oceans based on simulations with CCCma AGCM. The simulated effective radius generally decreases with height owing to aerosol sedimentation and deposition processes. The globally averaged values of the effective radii have a wide range from approximately 1 to 3.5 μm. The range is even larger for individual grid-points in the simulation. In contrast, the global mean effective variance has a relatively small range of variation in the lower atmosphere.

As a more simple alternative to the PLA approach, the dry sea-salt can be categorized into two modes, an accumulation mode with r_e=0.73 μm and a coarse mode with r_e=6.13 μm, both with the same v_e=0.65, based on climatologically representative results (Koepke et al., 1997), in which the proportion in the coarse mode is considered much larger than for the accumulation mode. We note that the AERONET results in Fig. 1 show wet sizes and yet the wet observed sea-salt effective radius is similar to the dry coarse mode effective size for sea-salt assumed above. Assuming the dry size and applying a humidity growth factor, that can be between about 1.5–5 (based on Eq. 5), will then likely lead to significant error.

For the growth of aerosol particles, the growth factor, η, is defined as the ratio of the

aerosol particle radius r at a specified $\mathcal{H}$ (the relative humidity normalized to unity) to the radius of the corresponding dry aerosol r_d,

$$\frac{r}{r_d} = \eta(r_d, \mathcal{H}) . \quad (4)$$

However, for dry particle size larger than 0.1 μm the dependence of the wet growth on dry size becomes very weak except for $\mathcal{H}$ close to 100%. All dry sizes studied show significant growth factors relative to dry, even for moderate $\mathcal{H}$ values, it is just that some variation of the growth dependence with initial dry size is noted for small aerosol sizes and high humidities. Therefore, the growth factor is simplified as $\eta(\mathcal{H})$. Zhang et al. (2005) has parameterized the sea-salt size dependence on salinity. A more practical way to parameterize the growth curve for our purposes is through the relative humidity, which, for example, has been done by Lewis and Schwartz (2006). Accordingly, the sea-salt growth factor is simply represented as

$$\eta(\mathcal{H}) = \frac{4.0}{3.7}\left(\frac{2-\mathcal{H}}{1-\mathcal{H}}\right)^{1/3} . \quad (5)$$

It is useful to consider the relationship between dry and wet particle sizes. The number of dry particles in the interval from r_d to r_d+dr_d is required to equal the number of wet particles in the interval from r to $r+dr$. That is, $n_d(r_d)dr_d=n(r)dr$. Consequently, the wet size distribution, $n(r)$, is related to the dry size distribution, $n_d(r_d)$, in the following way

$$n_d(r_d) \quad \rightarrow n(r) = n_d(r/\eta)\frac{d(r/\eta)}{dr} . \quad (6)$$

As the particles grow, the wet size distribution, $n(r)$, shifts toward larger radius sizes. If we assume the dry particle size distribution adheres to the log-normal distribution, then the wet size distribution will be distorted from the log-normal form for the dry particles, and vice versa.

ACPD
8, 5813–5845, 2008

A wet particle size weighted physical quantity $F(r)$ (e.g. extinction) can be calculated directly

$$\bar{F} = \int_0^\infty F(r)n(r)\,dr/N_0\,. \tag{7}$$

Based on Eq. (6), the manner in which the wet size distribution is related to the dry size distribution is specified, and $F(r)$ also can be calculated through the dry size distribution,

$$\bar{F} = \int_0^\infty F(\eta r_\mathrm{d})n_d(r_\mathrm{d})\,dr_\mathrm{d}/N_0\,. \tag{8}$$

The assumption that η is only a function of $\mathcal{H}$, according to Eq. (5) in combination with Eq. (6), leads to

$$r_\mathrm{e} = \frac{\int_0^\infty n(r)r^3dr}{\int_0^\infty n(r)r^2dr} \approx \frac{\eta^3\int_0^\infty n_d(r_d)r_d^3dr_d}{\eta^2\int_0^\infty n_d(r_d)r_d^2dr_d} = \eta r_{d\,e} \tag{9}$$

where $r_{d\,e}$ is the effective radius for dry size distribution. It can be easily shown that $v_e \approx v_{d\,e}$, where $v_{d\,e}$ is the effective variance for the dry aerosol.

Although physical properties can in principle be obtained for wet particle size distributions based on dry particle size distributions according to Eq. (8), this can be problematic for modeling. First, sea-salt particle sizes are considerably different from dry particle sizes at typical atmospheric relative humidities. The conversion from dry to wet sizes therefore needs to be sufficiently well known for accurate results. Further, the assumption of particle sizes in radiation calculations should be consistent with assumptions required for simulations of atmospheric transport processes, including sedimentation. Second, a radiation parameterization based on a limited number of values for the dry effective radius cannot adequately represent the physics that is associated with a potentially wide range of effective radii for wet particles. This generally results in poor results for optical properties with a limited number of interpolation points (see

ACPD
8, 5813–5845, 2008

detailed discussion for Fig. 4). Therefore it appears to a be a natural choice to directly calculate sea-salt optical properties based on wet size distributions in models.

In the early stages of aerosol climate modelling, it was not possible to predict the wet size distribution of sea-salt. At best, different fixed dry modes were considered. For example, the parameterization (Dobbie et al., 2003) was based on r_{de}. Today, more climate models are able to simulate the full wet size distribution, thus parameterizations for sea-salt optical properties should be consistent with the simulated wet sea-salt size distribution.

Based on the above argument, we propose a new approach which directly uses the wet particle distribution. Under the assumption of equilibrium, the growth factor can be calculated. This allows the determination of the components of dry aerosol in the wet particles. The corresponding volumes are $4/3\pi(r/\eta)^3$ and $4/3\pi(r-r/\eta)^3$ for the dry particle constituents and water, respectively. Based on this, the refractive index for the wet particles can be determined as the volume weighted mean of the refractive indexes for the dry particle and water. Therefore, the optical properties for sea-salt can be obtained for a given wet size distribution. It was found by Wang and Martin (2006) that the difference between volume mixing weight and molar mixing weight (Tang et al., 1997) is generally less than 1%.

3 Parameterization of sea-salt optical properties

The sea-salt optical properties typically required in radiative transfer calculations are the extinction coefficient, single scattering albedo and asymmetry factor for solar radiation and specific absorption coefficient for the longwave calculations.

The sea-salt optical depth is

$$\tau = \mathrm{WAC}/\psi \ , \tag{10}$$

ACPD
8, 5813–5845, 2008

where l is the geometrical path length, WAC is the wet aerosol content given by

$$\mathrm{WAC} = \frac{4\pi}{3} \int \rho_a n(r) r^3 \, dr \,, \tag{11}$$

where ρ_a is the mass density of the wet aerosols. WAC l is the aerosol loading. In Eq. (7) ψ is the specific extinction

$$\psi = \frac{\pi \int Q_{\mathrm{ext}}(\lambda, r) r^2 n(r) \, dr}{\mathrm{WAC}} \,, \tag{12}$$

where Q_{ext} is the extinction efficiency. The single scattering albedo, ω, specifies the fraction of total radiation interacting with a particle through scattering and absorption processes. It is defined as

$$\omega = \frac{\int Q_{\mathrm{sca}}(\lambda, r) r^2 n(r) \, dr}{\int Q_{\mathrm{ext}}(\lambda, r) r^2 n(r) \, dr} \,, \tag{13}$$

where Q_{sca} is the scattering efficiency.

The phase function, P, describes the angular distribution of scattered photons for scattering events. The normalized phase function is given by

$$P(\theta, \lambda) = \frac{\frac{\lambda^2}{2\pi^2} \int (i_1(\theta, r, \lambda) + i_2(\theta, r, \lambda)) n(r) \, dr}{\int Q_{\mathrm{sca}}(\lambda, r) r^2 n(r) \, dr} \,, \tag{14}$$

where θ is the scattering angle and i_1 and i_2 are the squares of the vertical and horizontal scattering amplitudes, respectively. The asymmetry factor is g, which is the integrated phase function weighted by the cosine of the scattering angle, and equates to one third of the first moment of the Legendre expansion of the phase function.

For the infrared, since the scattering is very weak, the radiative transfer equation can be dramatically simplified (Li, 2002; Bäumer et al., 2007) and only the absorptance depth, κ=WAC $l\xi$, is required, where ξ is the specific absorptance with

$$\xi = \psi(1 - \omega) \tag{15}$$

ACPD
8, 5813–5845, 2008

Equations Eqs. (11)–(14) are different from the corresponding formulae in Li et al. (2001), (Li and Min, 2002), Bäumer et al. (2007), since this work is directly based on the wet particle distribution. The upper bound in integrations for Eqs. (11)–(14) are set as 25 μm (Lewis and Schwartz, 2004).

The parameterization is based on five specified values for the effective radii for wet sea-salt size (0.73 μm, 1.75 μm, and 2.75 μm, 4.0 μm, and 6.13 μm). To obtain the optical properties for other values of effective radius, a Lagrangian interpolation technique can be employed.

It was generally believed that the variation in optical properties for effective variance is smaller than that for the effective radius. The corresponding radiative impact is also small for the effective variance. However, as shown in Fig. 2, GCM results give evidence for a relatively small variation in the effective variance for sea-salt in the atmosphere. According to the simulation results, the value of the sea-salt effective variance is generally larger than the commonly used value of 0.65, which was suggested by the simple dry two mode sea-salt scheme. The sensitivity of the sea-salt radiative forcing to observed variations in the effective variance will be discussed in a later section.

Humidity effects are considered based on Köhler theory with the water activity treated according to Tang et al. (1997). In the development of the parameterization, the humidity was considered to range from $\mathcal{H}$=0.45 to $\mathcal{H}$=0.99. The crystallization point for sea-salt is at about $\mathcal{H}$=0.45. Therefore, for humidity below $\mathcal{H}$=0.45 the sea-salt is considered to be dry. The parameterization for dry sea-salt optical properties is also provided based on the same effective radii and effective variances as the wet case. A dry sea-salt density of 2.24 g cm^{-3} is assumed.

For the optical properties in the solar range, the wavelengths from 0.2 to 4 μm are considered, with 25 single wavelength results. In the infrared, wavelengths from 4 to 1000 μm are considered, with 39 single wavelength results.

Aerosol optical properties as functions of wavelength are much smoother than gaseous optical properties. Therefore, even in a correlated k-distribution model, the aerosol optical properties are treated based on the band averaged results. For solar radiation,

the band average is obtained through a weighting of the results for each single wavelengths by the incoming solar spectrum at the top of the atmosphere. A weighting at the top of the sea-salt layer could also be considered but variations in sea-salt layer height and the variations in the gaseous concentrations make this a considerable task with minimal benefit.

The band averaged specific extinction coefficient, asymmetry parameter, and single scattering albedo for each band, i, are parameterized in the following way:

$$\psi_i = a_1^i + a_2^i \mathcal{H} + \frac{a_3^i}{(\mathcal{H} - 1.05)} \tag{16}$$

$$1 - \omega_i = b_1^i + b_2^i \mathcal{H} + \frac{b_3^i}{(\mathcal{H} - 1.05)} \tag{17}$$

$$g_i = c_1^i + c_2^i \mathcal{H} + \frac{c_3^i}{(\mathcal{H} - 1.05)}, \tag{18}$$

The parameterization coefficients a_n^i, b_n^i, and c_n^i are obtained by fitting to the exact Mie calculation results. For each value of a reference effective radius and each effective variance, a group of values for ψ_i, ω_i and g_i is provided. Results for a_n^i, b_n^i, and c_n^i are shown in Table 1 for a 4 band scheme.

Similar to the treatment for solar radiation, a band averaged weighted mean is applied to the longwave parameterization. The average value of specific absorptance for band i is defined as,

$$\xi_i = \int_{\Delta\lambda_i} \xi_\lambda B_\lambda(T) d\lambda \Big/ \int_{\Delta\lambda_i} B_\lambda(T) d\lambda \,. \tag{19}$$

where $B_\lambda(T)$ is the Planck function at wavelength λ, T is the temperature and $\Delta\lambda_i$ is the spectral interval for band i. Eq. (19) is physically similar to the Chandraskhar mean. T=273K is used in the weighting process since sea-salt is mostly located in the lower

ACPD
8, 5813–5845, 2008

atmosphere. Similarly, ξ_i is parametrized as

$$\xi_i = d_1^i + d_2^i \mathcal{H} + \frac{d_3^i}{(\mathcal{H} - 1.05)} \quad . \tag{20}$$

In contrast to the solar case, in which the spectral range of the 4 band scheme is a popular choice (Dobbie et al., 1999), there is significant variations in the band structures of different radiation algorithms for the longwave. Therefore, we do not provide any band averaged coefficients for the longwave (to obtain coefficients for individual band averaging, contact the corresponding author).

For solar wavelengths, it is found that the specific extinction shows a completely different behavior in response to changes in $\mathcal{H}$ for different values of the effective radius. However for the longwave, the behavior of specific absorptance in response to changes in $\mathcal{H}$ is very similar for different values of the effective radius. In the solar wavelength range, the ratio of the wavelength to particle size is small; while for the infrared the ratio is very large. From Mie theory the absorption is sensitive to this ratio only when the ratio is small. Although the absorptance coefficient is not sensitive to the effective radius in the longwave range, we still parameterize the results for five values of r_e in order to achieve consistency with the treatment for solar radiation.

It is found that the parameterized optical properties as functions of relative humidity match very well the results from exact Mie calculations for the five selected values of the effective radius r_e. The sea-salt optical properties for other values can be obtained through Lagrangian interpolation between the five values of r_e (Table 1). As an illustration, Fig. 3 shows interpolated results for sea-salt at r_e=1.5 μm and r_e=3 μm, both with v_e=0.65. It is found that the results of the parameterization generally agree very well with Mie calculations. The relative error of specific extinction coefficient is within 2%. The relative error for the asymmetry factor in band 4 at r_e=1.5 μm is within 1%. Overall, the results in Fig. 3 illustrate that the simple parameterization developed here is able to provide accurate values for the optical properties at arbitrary values of r_e.

In Fig. 3, it is interesting to note that the specific extinction coefficient is largest for

ACPD
8, 5813–5845, 2008

band 3. For aerosol with small size, usually the specific extinction is larger for smaller solar wavelength, thus the largest specific extinction would be expected to occur for band 1. We find this is true for the case with r_e=0.732. However for larger particle sizes, the back scattering becomes weaker and absorption becomes stronger. These two effects reduce the extinction at short wavelengths (where scattering is important) and enhance the extinction in the longer wavelengths (where absorption is important).

As mentioned above, in principle the aerosol optical properties can also be calculated based on dry size distributions according to Eq.(8). We can use the approximate relationship $r_e \approx \eta r_{de}$ with η given by Eq.(5) to determine optical properties in terms of r_{de}. Since η is strongly dependent on $\mathcal{H}$, for a fixed value of r_e, r_{de} is very sensitive to different values of $\mathcal{H}$. Also, for a given r_{de}, the Lagrangian interpolation can be used to create the sea-salt optical properties based on the pre-calculated results for a number of r_{de}. On the other hand, the two mode dry scheme Dobbie et al. (2003) cannot be expected to work in this case, since an interpolation based on only two points is not sufficiently accurate.

Here we used an 8-point Lagrangian interpolation method based on r_{de}=0.35, 0.5, 0.732, 1.2, 1.75, 2.75, 4 and 6.13 μm. Note that this includes the values r_{de}=0.732 and 6.13 μm which allows direct comparisons with results from the two mode dry scheme. Although more Lagrangian interpolation points are used than for the wet approach shown in Fig. 3, the results for the dry approach shown in Fig. 4 are overall poor compared to Fig. 3. In Fig. 4, the errors are relatively small for the asymmetry factor, but errors are large for the specific extinction coefficient, especially for large values of $\mathcal{H}$. These errors are partly related to the growth factor curve Eq. (5) which is used to determine the wet particle size for a given value of r_{de}. As mentioned, the growth factor is actually a function of $\mathcal{H}$ and particle size. However Eq. (5) is an averaged result for $r \geq 0.1$ μm. The sea-salt optical property calculation covers a wide range of different particle sizes, and the specific extinction is very sensitive to the small sizes.

The largest disagreement between both methods occurs for the single scattering co-albedo for bands 1 and 2, which are very weak absorbing bands. A detailed analysis

ACPD
8, 5813–5845, 2008

shows that the single scattering co-albedo in bands 1 and 2 is very sensitive to the dry r_{de}. For example, the difference in single scattering co-albedo in bands 1 and 2 is greater by one order of magnitude between r_{de}=0.35 and 1.75 μm in the lower $\mathcal{H}$ range. Even the 8-point Lagrangian interpolation cannot produce sufficiently accurate results under these conditions. In order to obtain accurate results, a much higher number of interpolation points would be required. However, from the direct wet method, the single scattering co-albedo is relatively smooth for different values of r_e as shown in Fig. 3 (<50% between r_e=1.5 and 3 μm). Therefore a few interpolation points can produce very accurate results for this method.

These results give evidence that simulations of sea-salt optical properties in climate models should be directly based on the wet size distribution. While it is possible to determine optical properties for dry particles based on wet particles, the opposite is less straightforward.

4 Physics of sea-salt radiative forcing

In order to quantify the radiative impact of sea-salt, we use a one-dimensional radiative transfer model. A one-dimensional radiative transfer model has the advantage over a General Circulation Model that it is much easier to analyze fundamental factors that determine the sea-salt direct forcing. More general results for sea-salt direct forcings in the global atmosphere were previously published by Ma et al. (2008).

The radiation algorithm of the Canadian Centre for Climate Modelling and Analysis is used here. This radiation model is a correlated k-distribution scheme for gaseous transmission (Li and Barker, 2005). For solar radiation, water vapor, CO_2, O_3, CH_4 and O_2 are considered for gaseous transmission. For longwave radiation, water vapor, CO_2, O_3, CH_4, O_3, CH_4, N_2O, CFC_{11}, and CFC_{12} are considered for gaseous transmission. For cloud and aerosol optical properties, there are 4 bands covering 0.2–4 μm and 9 bands covering from 4–1000 μm.

We will present forcing calculations for standard atmospheric profiles for mid-latitude

ACPD
8, 5813–5845, 2008

summer (MLS) and sub-Arctic winter (SAW) from McClatchey (1972). Selected solar and longwave radiative forcing results evaluated at the tropopause (200 mb) and surface will be presented. The sensitivity of forcing to the total loading, the surface albedo, the solar zenith angle and dependence of effective variance will be investigated.

First, the radiative forcing is calculated by using the sea-salt effective radius, effective variance and concentration profiles shown in Fig. 2. The vertically integrated loading shown in Fig. 2 is 0.136 gm^{-2}. By converting the wet concentration to dry concentration using equilibrium theory, we obtain a global oceanic mean dry sea-salt loading of 0.0133 gm^{-2}. This value is in good agreement with corresponding results from other models that were used in the AEROCOM project (Schulz et al., 2006). Note, that the concentration in Fig. 2 is the oceanic global mean, which is supposed to be higher than the global mean result since the sea-salt concentration is much lower over land.

In order to study the response of the forcing to the sea-salt loading, the sea-salt loading is varied from 0 to 2.0 gm^{-2} by scaling the concentration profile in Fig. 2. The observed maximum sea-salt loading is generally less than 0.2 gm^{-2} (Holben et al., 1998). Results are shown in Fig. 5. The forcing is defined as the difference in the net radiative flux at top of the atmosphere from two simulations, one with and the other without the aerosol. In Fig. 5, the solar zenith angle is set to be 53° which represents the daily average value. The surface albedo is set to 0.1.

It is shown in Fig. 5 that for an oceanic global mean loading of 0.136 gm^{-2}, the sea-salt solar radiative forcing at 200 mb and surface is about –10 Wm^2. The longwave forcing is about 1 Wm^{-2} at the surface and very small at 200 mb. It is interesting to note that the response in forcing is almost linearly related to the loadings, even for the high loading value of 0.5 gm^{-2}.

Generally the sea-salt optical depth in the simulations is very small compared to the total gaseous optical depth in the atmosphere, thus the radiative effect of sea-salt can be treated as a perturbation to the gaseous transmission. For sufficiently small perturbations, the response to a perturbed quantity is usually linear, even for a non-linear problem (see the later discussion of Eq. 21).

The simulated forcings are different for MLS and SAW despite identical aerosol properties in the calculations. In SAW, the atmosphere is drier. This produces less attenuation of solar radiance by water vapor above the layer with high sea-salt concentrations in the lower atmosphere. The relatively large incident solar flux produces a larger sea-salt forcing compared to MLS case. The sea-salt solar forcing is slightly lower at 200 mb in comparison with the forcing at the surface, for a given loading. At 200 mb, the solar forcing is mainly caused by the change of upward flux due to scattering by the sea-salt, while at the surface the solar forcing is mainly caused by the attenuation of the downward flux.

For the longwave, the radiative forcing is about one order of magnitude smaller than the corresponding solar forcing and is opposite in sign. The negative solar forcing means that the sea-salt acts to reduce the solar energy reaching the lower troposphere and thus causes a cooling, whereas the positive longwave forcing means that the sea-salt acts like a greenhouse gas in that it acts to prevent radiation loss to space. In a similar fashion to the solar forcing in which the change is mainly caused by the change in the upward flux, the longwave forcing at surface is caused by the change in the downward flux. Aerosols can reduce the downward flux of the longwave radiation and also can enhance the emission to the surface. The aerosol longwave direct forcing for the downward flux is determined by these two opposing factors.

The sea-salt longwave forcing is extremely small at 200 mb, generally less than $0.1\,\mathrm{Wm}^{-2}$. In order to explain the weak infrared forcing at the tropopause, a simple analytical approach has been developed. We first assume that the sea-salt is located in the lower atmosphere. For simplicity, we assume an isothermal longwave radiation source, i.e. a constant Planck function, B, for the temperature at the middle of the aerosol layer. The solution for the upward flux for longwave radiative transfer through such aerosol layers is given by (Li, 2002),

$$F^{\uparrow} = F_0^{\uparrow} e^{-\kappa/\mu_1} + (1 - e^{-\kappa/\mu_1})B \ , \tag{21}$$

where κ is the total absorptance depth with no aerosol contribution, $F^{\uparrow}$ is the upward

out-going flux from the considered layer and $F_0^{\uparrow}$ is the incoming flux from the surface, $1/\mu_1$ is the diffusivity factor, κ is the gaseous optical depth for the region. Assuming the aerosol layer with absorptance depth $\Delta\kappa$ ($\Delta\kappa \ll \kappa$), thus the forcing is

$$\Delta F^{\uparrow} = -F_0^{\uparrow} e^{-(\kappa+\Delta\kappa)/\mu_1} - (1 - e^{-(\kappa+\Delta\kappa)/\mu_1})$$
$$B + F_0^{\uparrow} e^{-\kappa/\mu_1} + (1 - e^{-\kappa/\mu_1})B \approx (F_0^{\uparrow} - B)e^{-\kappa/\mu_1}\Delta\kappa. \quad (22)$$

In the lower atmosphere, the difference in temperature between the atmosphere and surface is small. Therefore the values of $F_0^{\uparrow}$ and B are similar and the forcing is small. Generally $F_0^{\uparrow} > B$, thus the longwave forcing at the tropopause is positive, but the sign of the forcing may change if there is a strong temperature inversion in the lower atmosphere.

Equation (22) can be used to interpret the linear response of solar and longwave forcing to the loading as shown in Fig. 5. In the solar case, the forcing calculation is less straightforward compared to the longwave owing to scattering of solar radiation. However, a linearized treatment is appropriate for both forcings owing to relatively small perturbations (see previous discussion).

The thick lines in Fig. 5 show the sea-salt forcing under the same condition but with a low cloud appearing between 751 to 822 mb (the cloud liquid content is specified as $0.28\,\mathrm{gm}^{-3}$). The introduction of a cloud acts to reduced the sea-salt forcing for both cases because the back scattering of solar radiation is dominated by the cloud.

Similarly, the response of the solar forcing to variations in surface albedo is shown in Fig. 6. The aerosol concentration is given in Fig. 2 and the solar zenith angle is the same as for Fig. 5. The ocean is optically dark with an albedo that is generally less than 0.1. We note that sea-salt over highly reflective surfaces such as sea-ice can have a dramatic impact on the forcing, leading to large reductions as the albedo of the surface approaches unity. This is easy to understand for the solar forcing at the surface since the net solar flux at the surface diminishes as the surface albedo approaches unity. For the forcing at 200 mb, the reduction of forcing is mostly caused by a reduction in the

ACPD
8, 5813–5845, 2008

difference in the reflected upward fluxes (with and without aerosol input). Over a high albedo, more photons are reflected back to the space, and so the effect of reflection by the aerosol layer does not make a significant difference to the total reflection, so the effect on the forcing is minimal.

The sea-salt solar forcing also varies with the solar zenith angle. For Fig. 7, the sea-salt input is the same as for Fig. 6 but with a solar zenith angle varying from 0 to 90° and for a surface albedo of 0.1. It is found for both the MLS and SAW that the solar forcing is positive for zenith angles less than about 30°. For larger solar zenith angles, the solar forcing becomes negative. Therefore the commonly accepted concept of negative sea-salt solar forcing does not apply under these circumstances. The sign of sea-salt forcing is highly dependent on the direction of incoming solar radiation. When the solar zenith angle is small, the scattering by the sea-salt is mostly downwards. Effects of sea-salt on downward scattering are relatively small so that the fluxes do not depend strongly on the amount of sea-salt. However, the solar flux reflected by the surface and escaping to space is reduced by the absorption in the sea-salt layer at near infrared bands. For larger solar zenith angles, the up-scatter from the sea-salt increases as the incident angle increases. In this case, the strong forward scattering in the phase function begins to contribute to the up-scatter and hence reflection.

The negative solar forcing does not increase monotonically with solar zenith angle, and for very large angles the magnitude of the forcing becomes very small. Two competing factors are important. As the solar zenith angle gets larger, the incoming radiation is more horizontal in direction. This is associated with an increased probability that the strong forward diffraction peak will contribute to the up-scatter and reflection. On the contrary, the increased solar zenith angle decreases the flux to the sea-salt layer. In the limit of grazing incident radiation, the flux and consequently forcing tends to zero. The result of the competition of these two processes is a maximum negative forcing at about 75°.

The positive solar forcing for small solar zenith angle may partly explain small negative sea-salt solar forcing observed in the tropics, since small solar zenith angles occur

ACPD
8, 5813–5845, 2008

more frequently in the tropics compared to the extratropics. Of course, another very important reason for small solar sea-salt forcings in the tropics is the relatively low wind speed compared to the extratropics which are generally associated with lower production rates for sea-salt particles.

The aerosol effective radius plays a critical role in radiative transfer. This is particularly true for the solar spectrum. For a given aerosol burden, smaller particles reflect more solar energy to space relative to large particles. This is because smaller particles have a much smaller forward scattering peak. However, the differences in forcing for changes in effective variance are not believed to be important for radiative forcing (Chýlek and Wong, 1995). To our knowledge, this has not been verified with calculations using observed values of v_e in the real atmosphere. In order to investigate the impact of v_e on forcings, we used the same sea-salt input as for Fig. 5, but replaced the v_e profile shown in Fig. 2 with two constant values v_e=0.4 and 0.8, respectively. The differences in forcings for v_e=0.4 (v_e=0.8) relative to the results for Fig. 5 with a vertically varying v_e taken from Fig. 2 are shown in Fig. 8. According to Fig. 8, results are not sensitive to v_e for both solar and longwave. The maximum difference is less than 0.2 Wm^{-2}. Compared to the results in Fig. 5, the relative difference in the forcings is very small.

Large values of v_e indicate the presence of large and small particles. Compensating effects of small and large particles on the solar forcing leads to a weak sensitivity of the forcing to effective variance. We therefore use v_e=0.65, as presented in Table 1.

5 Conclusions

We have presented a new parameterization of the solar and longwave optical properties for sea-salt aerosol. The solar part of the parameterization represents an improvement over previous work (Dobbie et al., 2003) by using an efficient method for the calculation of the optical properties based on the wet sea-salt aerosol size distribution. For the longwave, we note this to be the first parameterization for sea-salt

ACPD
8, 5813–5845, 2008

optical properties to appear in the literature. The parameterization is based on results from Mie calculations for five values of the effective radius. A Lagrangian interpolation is proposed to obtain results for other values of the effective radius. Results for sea-salt aerosol optical properties are in better agreement with Mie calculations for a wide range of aerosol particle sizes compared to a two mode scheme based on dry sea-salt aerosol size distribution.

It is shown that the effective variance has only a small impact on sea-salt radiative forcings, based on values of the effective variance varying from 0.4 to 0.8 for the studied atmospheric profiles. We have therefore used a single value for this parameterization of v_e=0.65.

Variations in sea-salt size distributions in terms of effective radius and sea-salt column loading have been shown to have a strong impact on radiative forcings. Both the sea-salt solar forcing and longwave forcing were shown to respond nearly linearly to the sea-salt loading for a realistic range of values. The nearly linear response can be attributed to the relatively small perturbation of sea-salt aerosol to the radiative transfer process in the atmosphere. It is further confirmed that the surface albedo can substantially affect the sea-salt solar forcing, with the forcing diminishing toward zero as the surface albedo tends to unity.

It is interesting to note that sea-salt can generate a positive solar forcing when the solar zenith angle is less than 30°. For small solar zenith angles, the scattering in the sea-salt layer is mostly forward and downward with only small effects of sea-salt on back scattering of the solar radiation. The absorbing components of sea-salt, however, cause a reduction in the solar flux reaching the surface and therefore may lead to a positive solar forcing. These results should be emphasized since traditionally it is assumed that the sea-salt solar forcing is negative. Also, it is interesting to note that the sea-salt longwave forcing can be negative when there is a large temperature inversion in the lower atmosphere. We note that in general the solar forcing is greater than the longwave forcing by an order of magnitude for the results presented.

This work offers a versatile and efficient parameterization for sea-salt at solar and

ACPD
8, 5813–5845, 2008

longwave wavelengths that is appropriate for implementation in GCMs. We note that the parameterization presented in the paper can be modified for other band structures. Parameterization coefficients in Eqs. (16–18) for the 25 single wavelength values between 0.2 to 4 μm and the coefficients in Eq. (20) for 39 single wavelength values between 4 to 50 μm are available from the authors.

Acknowledgements. We are grateful to C. Reader for her helpful comments.

References

Alley, R. B.: The Younger Dryas cold interval as viewed from central Greenland, Quaternary Science Reviews, 19, 213–226, 2000. 5815

Bäumer, D., Lohmann, U., Lesins, G., Li, J., and Croft, B.: Parameterizing the optical properties of carbonaceous aerosols in the Canadian Centre for Climate Modeling and Analysis Atmospheric General Circulation Model with impacts on global radiation and energy fluxes, J. Geophys. Res., 112, D10207, doi:10.1029/2006JD007319, 2007. 5815, 5822, 5823

Chýlek, J. and J. G. D. Wong: Effect of absorbing aerosols on global radiation budget, J. Geophys. Res. Lett., 22, 929–931, 1995. 5832

Haywood, J. M., Ramaswamy, V., and Donner, L. J.: A limited-area-model case study of the effects of sub-grid scale variations in relative humidity and cloud upon the direct radiative forcing of sulfate aerosol Geophys. Res. Lett., 24, 143–146, 1997. 5815

Dobbie, J. S., Li, J., and Chýlek, P. : Two and Four Stream Optical Properties for Water Clouds and Solar Wavelengths, J. Geophys. Res., 104, 2067–2079, 1999. 5825

Dobbie, J. S., Li, J. Harvey, R., and Chýlek, P.: Sea-salt optical properties and GCM forcing at solar wavelengths, Atmos. Res., 65 (special issue for aerosol), 211–233, 2003. 5815, 5821, 5826, 5832

Holben, B. N., Eck, T. F., Slutsker, I., Tanre, D., Buis, J. P., Setzer, A., Vermote, E., Reagan, J. A., Kaufman, Y., Nakajima, T., Lavenu, F., Jankowiak, I., and Smirnov, A.: AERONET - A federated instrument network and data archive for aerosol characterization, Rem. Sens. Environ., 66, 1–16, 1998. 5818, 5828

Koepke, P., Hess, M., Schult, I., and Shettle, E. P.: Global Aerosol Data Set, Report No. 243 of the Max-Planck-Institut für Meteorologie, Hamburg, ISSN 0937–1060, 1997. 5818

Lewis, E. R. and Schwartz, S. E.: Sea salt aerosol production: Mechanisms, methods, measurements and models – a critical review, Geophysical Monograph, 152, pp. 413, 2004. 5816, 5823

Lewis, E. R. and Schwartz, S. E.: Comment onsize distribution of sea-salt emissions as a function of relative humidity, Atmos. Environ., 40, 591–592, 2006. 5819

Li, J., Wong, J. G., D., Dobbie, J. S., and Chýlek, P.: Parameterization of the optical properties and growth of sulfate aerosols, J. Atmos. Sci., 58, 193–209, 2001. 5823

Li, J.: Accounting for unresolved clouds in a 1D infrared radiative transfer model, Part I: Solution for radiative transfer, cloud scattering, and overlap, J. Atmos. Sci., 59, 3302–3320, 2002. 5822, 5829

Li, J. and Min, Q. : Parameterization of the optical properties of sulfate aerosols in the in the infrared, J. Atmos. Sci., 59, 3130–3140, 2002. 5815, 5823

Li, J. and Barker, H. W.: A radiation algorithm with correlated k-distribution. Part I: local thermal equilibrium, J. Atmos. Sci., 62, 286–309, 2005. 5827

Li, J., Scinocca, J., Lazare, M., McFarlane, N., von Salzen, K., and Solheim, L.: Ocean surface albedo and its impact on radiation balance in climate models, J. Climate, 19, 6314–6333, 2006. 5815

Ma, X.Y., and von Salzen, K.: Dynamics of the sulphate aerosol size distribution on a global scale, J. Geophys. Res., 111, D08206, doi:10.1029/2005JD006620, 2006. 5817

Ma, X.Y., von Salzen K., and Li, J.: Modelling sea-salt aerosol and its direct and indirect effects, Atmos. Chem. Phys., 8, 1311–1327, 2008, http://www.atmos-chem-phys.net/8/1311/2008/. 5818, 5827

McClatchey, R. A., Fenn, R. W., Selby, J. E. A., Volz F. E., and Garing, J. S.: Optical properties of the atmosphere, 3rd ed., AFCRL-72-0497, 108 pp. [NTIS N7318412], 1972. 5828

O'Dowd, C. D., Lowe, J. A., Smith, M. H., and Kaye, A. D.: The relative importance of non-sea-salt sulphate and sea-salt aerosol to the marine cloud condensation nuclei population: An improved multi-component aerosol-cloud droplet parameterization, Quart. J. R. Meteorol. Soc., 125, 1295–1313, 1999. 5815

Penner, J. E., Andrea, M., Annegarn, H., Barrie, L., Feichter, J., Hegg, D., Jayaraman, A., Leaitch, R., Murphy, D., Nganga, J., and Pitari, G.: Aerosols, their direct and indirect effects, Climate Change 2001: The Scientific Basis, Contribution of Working Group I to the Third Assessment Report of the Intergovernmental Panel on Climate Change edited by: Houghton, J. T., Y. Ding, D. J. Griggs, M. Noguer, P. J. van der Linden, X. Dai, K. Maskell, and C. A.

Johnson, Cambridge University Press, Cambridge, UK and New York, NY, USA, pp. 289, 2001. 5815

Schulz, M., Textor, C., Kinne, S., Balkanski, Y., Bauer, S. Berntsen, T., Berglen, T., Boucher, O., Dentener, F., Grini, A., Guibert, S., Iversen, T., Koch, D., Kirkevag, A., Liu, X., Montanaro, V., Myhre, G., Penner, J., Pitari, G., Reddy, S., Seland, O., Stier, P., and Takemura, T.: Radiative forcing by aerosols as derived from the AeroCom present-day and pre-industrial simulations, Atmos. Chem. Phys., 6, 5225–5246, 2006, http://www.atmos-chem-phys.net/6/5225/2006/. 5828

von Salzen, K.: Piecewise log-normal approximation of size distributions for aerosol modelling, Atmos. Chem. Phys., 6, 1351–1372, 2006, http://www.atmos-chem-phys.net/6/1351/2006/. 5817

Tang, I. N., Tridico A. C. and Fung, K. H.: Thermodynamic and optical properties of sea-salt aerosols, J. Geophys. Res., 102, 23 269–23 275, 1997. 5816, 5821, 5823

Wang, J. and Martin, S. T. : Satellite characterization of urban aerosols: importance of including hygroscopicity and mixing state in the retrieval algorithms, J. Geophys. Res., 112, D17203, doi:10.1029/2006JD008078, 2006. 5821

Tang, I. N., Tridico, A. C., and Fung, K. H.: Contribution of sea salt aerosol to the planetary clear-sky albedo Tellus Series B, 49, 72–79, 1997 5815

Satellite characterization of urban aerosols: importance of including hygroscopicity and mixing state in the retrieval algorithms, J. Geophys. Res., 112, D17203, doi:10.1029/2006JD008078, 2006.

Zhang, K. M., Knipping, E. M., Wexler, A. S., Bhave, P. V., and Tonnesen, G. S.: Size distribution of sea-salt emissions as a function of relative humidity, Atmos. Env. 39, 3373–3379, 2005.

Table 1. Coefficients for the sea-salt parameterization in Equations (16)–(18) for 4 band scheme.

The band ranges are 0.2–0.69, 0.69–1.19, 1.19–2.38, 2.38–4 μm for bands i=1, 2, 3, 4										
r_e (μm)	i	a_1^i (m^2g^{-1})	a_2^i (m^2g^{-1})	a_3^i (m^2g^{-1})	b_1^i	b_2^i	b_3^i	c_1^i	c_2^i	c_3^i
	1	1.666	7.905e–1	–1.091e–2	9.849e–8	5.287e–8	–2.613e–10	0.7320	5.843e–2	–4.335e–4
0.732	2	1.563	5.111e–1	–6.509e–3	9.452e–6	7.254e–6	–5.900e–8	0.7400	5.493e–2	–3.577e–4
	3	1.127	2.036e–1	–2.468e–3	6.303e–4	6.621e–4	–6.863e–6	0.7309	4.953e–2	–3.079e–4
	4	0.5313	8.481e–2	–1.571e–3	1.592e–1	1.407e–1	–1.219e–3	0.6916	1.829e–2	1.109e–4
	1	0.6171	3.427e–1	–5.142e–3	2.721e–7	1.174e–7	–6.352e–10	0.7527	4.123e–2	–3.657e–4
1.75	2	0.6814	3.584e–1	–5.159e–3	2.322e–5	1.215e–5	–5.711e–8	0.7397	5.396e–2	–4.271e–4
	3	0.6981	2.848e–1	–3.756e–3	1.183e–3	7.544e–4	–5.243e–6	0.7461	5.933e–2	–4.090e–4
	4	0.5600	1.174e–1	–1.420e–3	1.281e–1	7.231e–2	–6.946e–4	0.7678	4.423e– 2	–8.447e–5
	1	0.3724	2.035e–1	–3.073e–3	4.087e–7	2.476e–7	–1.001E-10	0.7767	3.247e–2	–2.777e–4
2.75	2	0.4017	2.240e–1	–3.357e–3	3.895e–5	2.012e–5	–6.951e–8	0.7508	4.330e–2	–3.837e–4
	3	0.4371	2.213e–1	–3.127e–3	1.910e–3	1.020e–3	–5.294e–6	0.7458	5.731e–2	–4.404e–4
	4	0.4314	1.324e–1	–1.499e–3	1.363e–1	5.150e–2	–4.730e–4	0.7825	5.412e–2	–1.750e–4
	1	0.2506	1.349e–1	–2.031e–3	5.761e– 7	3.841e–7	1.526E-10	0.7955	2.940e–2	–2.315e–4
4	2	0.2640	1.459e–1	–2.208e–3	5.802e–5	3.117e–5	–1.263e–7	0.7693	3.413e–2	–3.064e–4
	3	0.2856	1.567e–1	–2.313e–3	2.869e–3	1.457e–3	–6.245e–6	0.7519	5.013e–2	–4.260e–4
	4	0.3090	1.244e–1	–1.484e–3	1.535e–1	3.939e–2	–3.183e–4	0.7887	5.904e–2	–2.477e–4
	1	0.1648	8.798e–2	–1.321e–3	8.234e–7	5.999e–7	3.837e–10	0.8115	2.870e–2	–2.136e–4
6.13	2	0.1707	9.234e–2	–1.394e–3	8.593e–5	4.950e–5	–2.380e–7	0.7923	2.853e–2	–2.333e–4
	3	0.1801	1.001e–1	–1.513e–3	4.364e–3	2.288e–3	–9.536e–6	0.7692	3.944e–2	–3.547e–4
	4	0.1986	9.837e–2	–1.299e–3	1.820e–1	3.091e–2	–1.638e–4	0.7973	5.830e–2	–3.188e–4

ACPD
8, 5813–5845, 2008

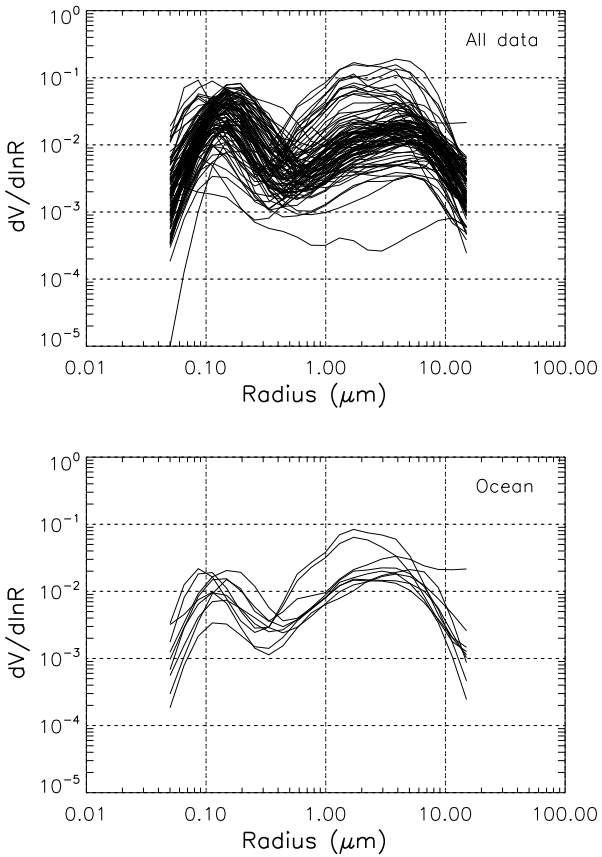

Fig. 1. Aerosol size distributions from AERONET for all stations (upper panel) and for stations only over ocean (lower panel).

ACPD
8, 5813–5845, 2008

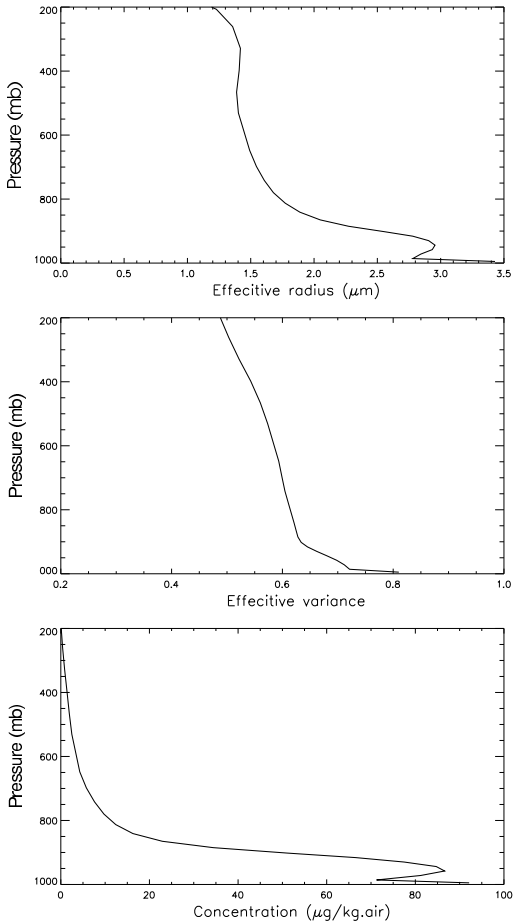

Fig. 2. Vertical profiles of the oceanic global mean effective radius (top panel), effective variance (middle panel) and concentration (bottom panel) taken from GCMs calculations.

ACPD
8, 5813–5845, 2008

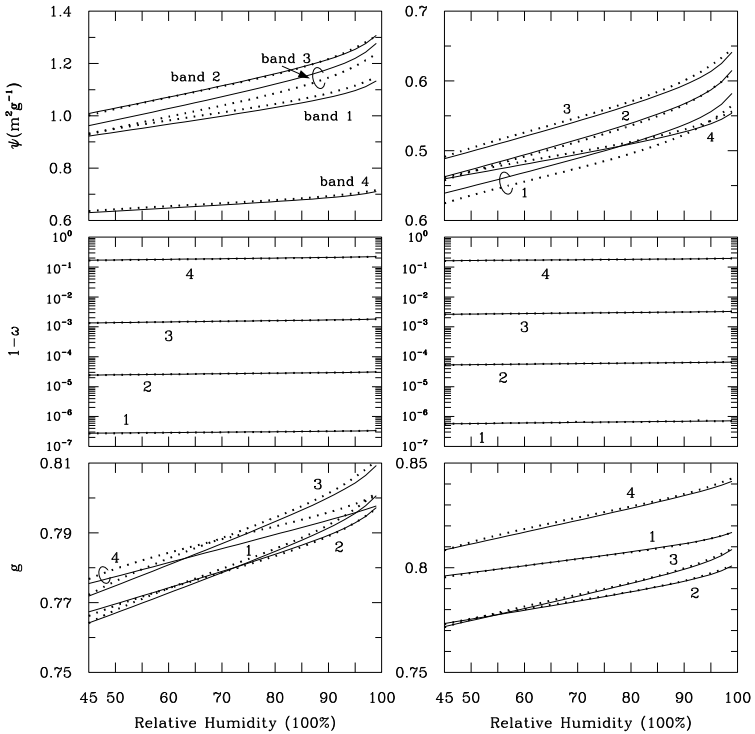

Fig. 3. The variation of the optical properties of specific extinction coefficient, single scattering co-albedo and asymmetry parameter as functions of relative humidity for sea-salt. Two effective radii are considered as r_e=1.5 μm (left column) and r_e=3 μm (right column), both for an effective variance v_e=0.65. The theoretical calculations are shown as solid lines and the results by the proposed parameterization with a 5-point Lagrangian interpolation are indicated by dotted lines.

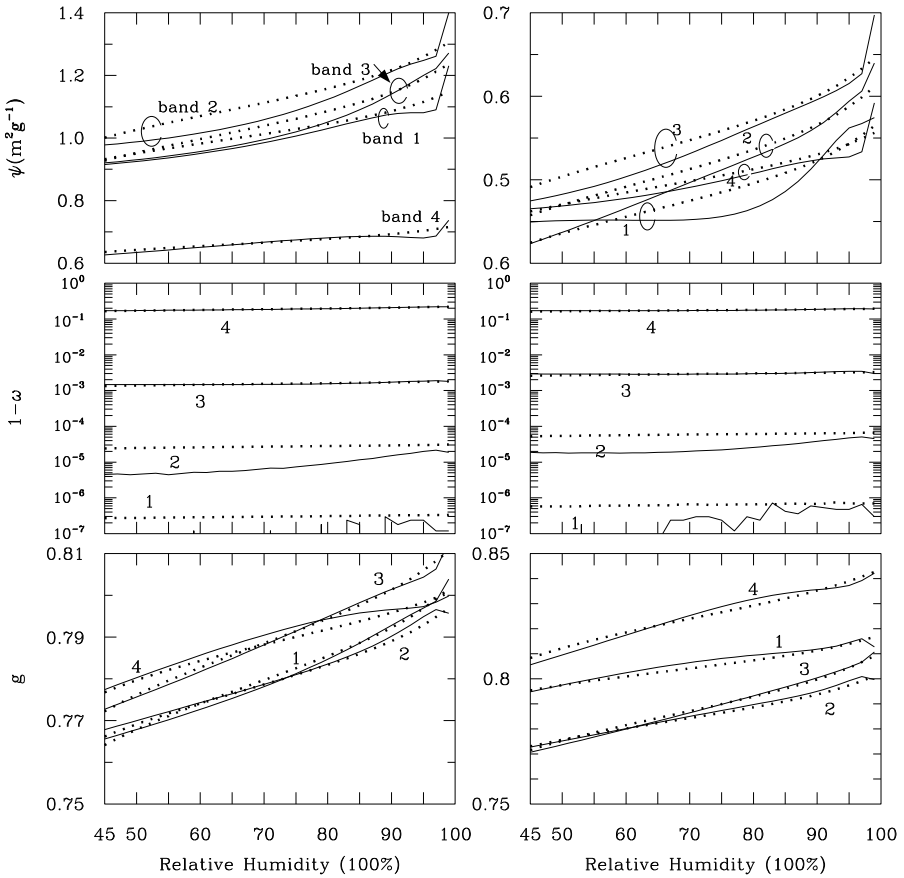

Fig. 4. The same as Fig. 3 but parameterization is based on a dry aerosol size distribution with an 8-point Lagrangian interpolation.

ACPD
8, 5813–5845, 2008

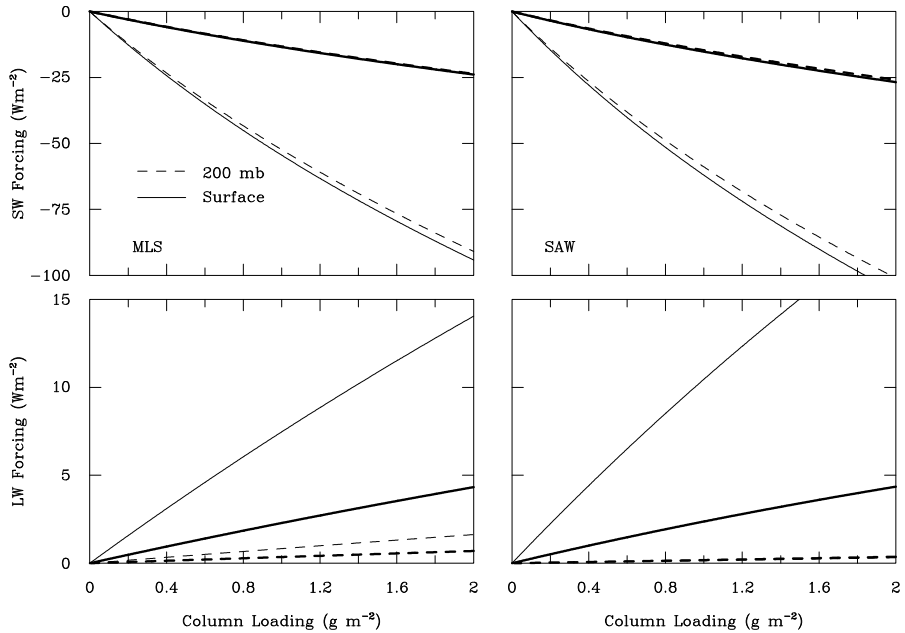

Fig. 5. The sea-salt solar radiative forcing (upper panels) and longwave radiative forcing (lower panels) at 200 mb (dashed lines) and at surface (solid lines). Two atmospheric profiles of MLS (middle latitude summer) and SAW (sub-Arctic winter) are considered. The sea-salt vertical profiles of r_e, v_e and concentration are the same as for Fig. 2. Concentrations are scaled linearly relative to the profiles shown in Fig. 2 (as discussed in the text). The corresponding thick lines refer to results for the same input conditions but with a low cloud located between 751 to 822 mb with a liquid water content of 0.28 gm^{-3}.

ACPD
8, 5813–5845, 2008

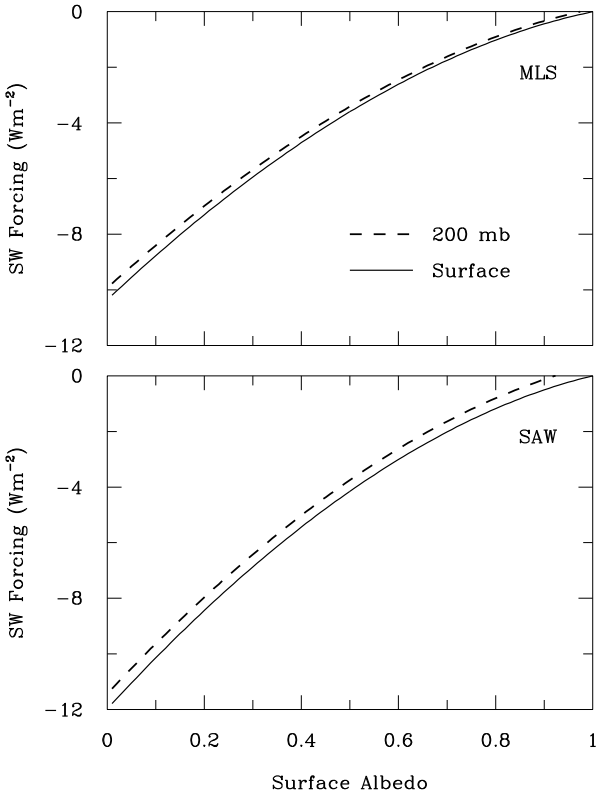

Fig. 6. The sea-salt solar radiative forcing versus surface albedo. The atmospheric profile and sea-salt vertical profiles are the same as in Fig. 2. The solar zenith angle is 53°.

ACPD
8, 5813–5845, 2008

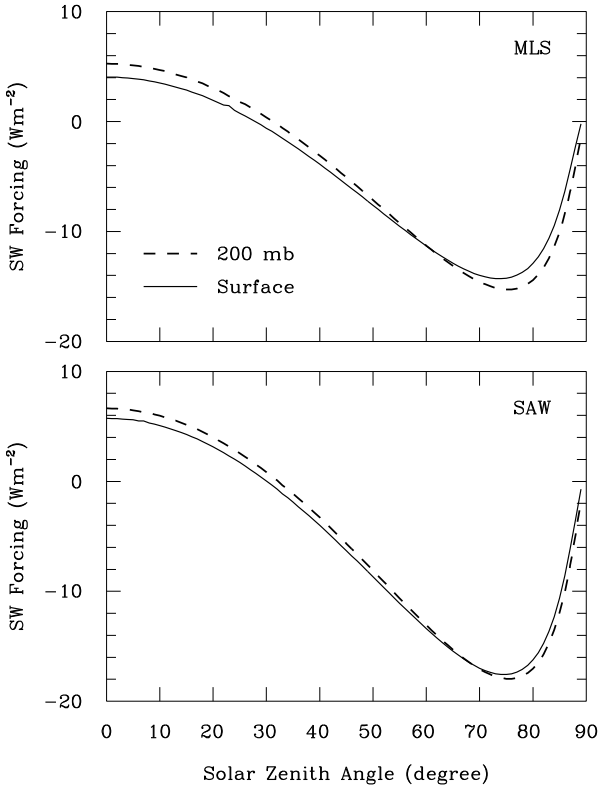

Fig. 7. The sea-salt solar radiative forcing versus solar zenith angle. The atmospheric profile and sea-salt vertical profiles are the same as for Fig. 2. A surface albedo of 0.1 is assumed.

ACPD
8, 5813–5845, 2008

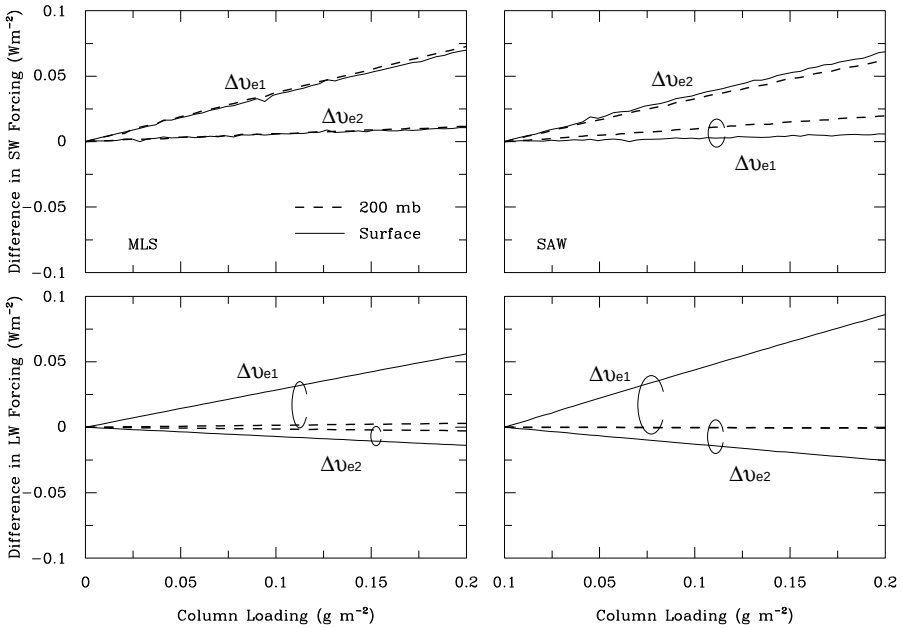

Fig. 8. The differences in radiative forcing between constant v_e against the results of Fig. 5 (clear sky case) with v_e profile shown in Fig. 2. All other input parameters are the same as those for Fig. 5 (clear sky case). $\Delta v_e1 = v_e(0.4) - v_e$(Fig.2) represents the results for constant v_e=0.4 relative to the results for v_e from the profile shown in Fig. 2. $\Delta v_e2 = v_e(0.8) - v_e$(Fig.2) represents the results for constant v_e=0.8 relative to the results for v_e from the profile shown in Fig. 2.